Biogeosciences

New insights into $f\mathrm{CO_2}$ variability in the tropical eastern Pacific Ocean using SMOS SSS

C. Walker Brown, J. Boutin, and L. Merlivat

Sorbonne Universités (UPMC, Univ Paris 06)-CNRS-IRD-MNHN, LOCEAN Laboratory, 4 place Jussieu, 75005 Paris, France

Correspondence to: C. Walker Brown (christopher.brown@locean-ipsl.upmc.fr)

Abstract. Complex oceanic circulation and air–sea interaction make the eastern tropical Pacific Ocean (ETPO) a highly variable source of $\mathrm{CO_2}$ to the atmosphere. Although the scientific community have amassed 70 000 surface fugacities of carbon dioxide ($f\mathrm{CO_2}$) data points within the ETPO region over the past 25 years, the spatial and temporal resolution of this data set is insufficient to fully quantify the seasonal to interannual variability of the region, a region where $f\mathrm{CO_2}$ has been observed to fluctuate by $> 300\,\mu\mathrm{atm}$.

Upwelling and rainfall events dominate the surface physical and chemical characteristics of the ETPO, with both yielding unique signatures in sea surface temperature and salinity. Thus, we explore the potential of using a statistical description of $f\mathrm{CO_2}$ within sea-surface salinity–temperature space. These SSS/SST relationships are based on in situ surface ocean $\mathrm{CO_2}$ atlas (SOCAT) data collected within the ETPO. This statistical description is then applied to high-resolution (0.25°) Soil Moisture and Ocean Salinity (SMOS) sea surface salinity (SSS) and Operational Sea Surface Temperature and Sea Ice Analysis (OSTIA) sea surface temperature (SST) in order to compute regional $f\mathrm{CO_2}$. As a result, we are able to resolve $f\mathrm{CO_2}$ at sufficiently high resolution to elucidate the influence that various physical processes have on the $f\mathrm{CO_2}$ of the surface ETPO.

Normalised (to 2014) oceanic $f\mathrm{CO_2}$ between July 2010 and June 2014 within the entire ETPO was 39 (±10.7) µatm supersaturated with respect to 2014 atmospheric partial pressures, and featured a $\mathrm{CO_2}$ outgassing of 1.51 (±0.41) $\mathrm{mmol\,m^{-2}\,d^{-1}}$. Values of $f\mathrm{CO_2}$ within the ETPO were found to be broadly split between the Gulf of Panama region and the rest of the tropical eastern Pacific Ocean. The northwest, central and offshore regions were supersaturated, with wintertime wind-jet-driven upwelling found to constitute the first-order control on $f\mathrm{CO_2}$ values. This contrasts with the southeastern/Gulf of Panama region, where heavy rainfall combined with rapid stratification of the upper water column act to dilute dissolved inorganic carbon, and yield $f\mathrm{CO_2}$ values undersaturated with respect to atmospheric fugacities of $\mathrm{CO_2}$.

1 Introduction

Perturbations to the global carbon cycle caused by anthropogenically driven increases in atmospheric partial pressures of $\mathrm{CO_2}$ ($p\mathrm{CO_2}$) produce an acute requirement to understand inter-reservoir carbon fluxes (Le Quéré et al., 2015). However, assessing these fluxes, especially the flux between the atmosphere and surface ocean, is challenging, as $p\mathrm{CO_2}$ within the oceanic reservoir varies considerably both spatially and temporally. Fortunately, considerable effort has been made in recording oceanic $p\mathrm{CO_2}$ (or fugacity – $f\mathrm{CO_2}$) over the past 50 years, with roughly 10 million individual measurements of global surface ocean $p\mathrm{CO_2}$ taken, processed, flagged and assembled into two large data sets: the surface ocean $\mathrm{CO_2}$ atlas (SOCAT) and Lamont-Doherty Earth Observatory (LDEO) carbon dioxide database (Bakker et al., 2014; Takahashi et al., 2014). Both databases make heavy use of "vessel-of-opportunity"-derived $p\mathrm{CO_2}$ data, resulting in a heterogeneous data set with the majority of measurements collected within the tight confines of commercial shipping lanes.

The first stage in efforts to estimate large-scale air–sea fluxes requires the extrapolation of these discrete surface

pCO$_2$ observations over large areas of surface ocean. Completing a basic extrapolation of these vessel-of-opportunity-based data results in a spatially patchy pCO$_2$ field, as seen in the 1° gridded product available from SOCAT (Bakker et al., 2014). Therefore, in order to achieve improved spatial coverage, a frequently used solution is to fit data-driven diagnostic models (e.g. Feely et al., 2006; Park et al., 2010; Rödenbeck et al., 2013). These models use observed correlations between physical properties and the pCO$_2$ observed under these conditions. In addition, statistical criteria, based on the surface ocean observations (for example, satellite imagery) and/or neural networks, have been used to identify biogeochemical provinces in order to improve the accuracy of the extrapolated field (Boutin et al., 1999; Cosca et al., 2003; Rangama et al., 2005; Landschützer et al., 2014). Although the quality of these extrapolation methods has been refined over the past few years, in part due to the increasing number of in situ measurements, the interannual variability of the global air–sea CO$_2$ flux obtained using different data-driven methods still substantially differs, and further work is required to unify our estimates and improve understanding of this air–sea flux.

The recent (2010–present) availability of sea surface salinity from the Soil Moisture Ocean Salinity (SMOS) mission has provided a new tool in statistically modelled pCO$_2$ studies, as now the relationship between surface temperature, salinity, density and pCO$_2$ can be utilised in high-resolution statistical descriptions of pCO$_2$ within temperature and salinity (TS) space. It is this relationship that is explored within this paper in order to quantify inter- and intraannual variability within the oceanographically complex eastern tropical Pacific Ocean (ETPO) region between 4 and 18° N, and east of 95° W (Fig. 1).

The ETPO region is influenced by northern and southern hemispheric trade winds, the doldrums, strong seasonal wind jets, heavy rainfall, strong solar heating and the El Niño–Southern Oscillation (ENSO; Kessler, 2006). Within the ETPO the intertropical tropical convergence zone (ITCZ) is neither zonally oriented, nor spatially fixed over the course of a year; thus wind fields are highly variable in both strength and direction (Kessler, 2006). Further wind variability is introduced by low-altitude jets blowing through three low-elevation gaps in the Central American Cordillera, with these jets observed predominantly between November and February (Kessler, 2002, Fig. 1 – schematically represented by orange arrows). These strong jet winds are generated from the pressure gradient force resulting from high-pressure synoptic mid-latitude weather systems transiting North America towards the low-pressure equatorial Pacific during the winter months (Chelton et al., 2001). Jet wind velocities of up to 20–30 ms^{-1} have been observed within the three gulfs, extending from the shoreline to at least 500 km into the ETPO (Chelton et al., 2001). The alignment of these jets is mainly meridional in the Gulf of Panama and Tehuantepec, and more zonal in the Gulf of Papagayo (Fig. 1). These jet winds result
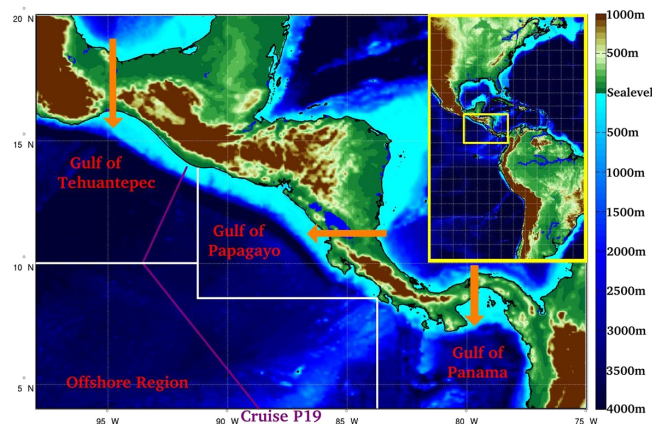

Figure 1. The topography of the eastern tropical Pacific Ocean and Isthmus of Panama, plotted using the General Bathymetric Chart of the Oceans (GEBCO; http://www.gebco.net/) bathymetry. The three gulfs within the region, Panama (84° W from coastline of Panama), Papagayo (84 to 91° W, north of 8° N) and Tehuantepec (west of 91° W, north of 10° N), and the offshore region, are marked in white. The transect of WOCE cruise P19 is indicated in purple. The paths of jet winds are marked by orange arrows.

in strong wintertime upwelling in each of the three basins, with the northerly jet winds in the gulfs of Tehuantepec and Panama promoting Ekman upwelling (Kessler, 2006). At 9° N, 90° W, the quasi-permanent anticyclonic Costa Rica thermocline dome is energised by the westerly jet winds in the Gulf of Papagayo, again, resulting in upwelling (Fig. 1; Kessler, 2002). However, the pressure disequilibrium that spawns these jet winds builds and subsides quickly (on a sub-weekly timescale), resulting in a highly fluctuating jet wind field, and non-linearities in the oceanic (and hence upwelling) response to these episodic events (Kessler, 2006). Recent studies have shown that satellite sea surface salinity (SSS) data are very well suited to capture the variability of these high-SSS events (Grodsky et al., 2014; Reul et al., 2013).

During summertime, these jet winds are rare, and the northward deflection of the ITCZ over the ETPO results in very high levels of precipitation, particularly within the Gulf of Panama (Fig. 1; Alory et al., 2012). The effect of this rainfall is a strong freshening and stratification of the surface, especially in the Gulf of Panama region. For this reason, the Gulf of Panama is often referred to as the "Pacific fresh pool", with salinities of < 30 frequently observed (Alory et al., 2012).

2 Data and methods

2.1 Observations of in situ $f\mathrm{CO_2}$, dissolved inorganic carbon and atmospheric $\mathrm{CO_2}$

We use SOCAT data as the basis of a statistical description of $p\mathrm{CO_2}$ within the ETPO. All $\mathrm{CO_2}$ data within the SO-CAT database are recorded as fugacity of $\mathrm{CO_2}$ ($f\mathrm{CO_2}$); a measure of $p\mathrm{CO_2}$ that is corrected for the non-ideal-gas behaviour that carbon dioxide displays (Bakker et al., 2014). In this study we will use fugacity of $\mathrm{CO_2}$, owing to the improved accuracy of this measure over $p\mathrm{CO_2}$. The logistical importance of the region has proven beneficial, producing a large database of $f\mathrm{CO_2}$/SSS/sea surface temperature (SST) observations, with $\sim 70\,000$ surface carbon, temperature and salinity data points collected between 1991 and 2011 (within the region depicted in Fig. 1). We use data (converted from $p\mathrm{CO_2}$ to $f\mathrm{CO_2}$) collected between 1991 and 2013 within the LDEO v2013 database as a semi-independent data set to test our SOCAT-based statistical description of $f\mathrm{CO_2}$ within TS space (Takahashi et al., 2014). The LDEO database extends 2 years longer than SOCAT, making it a useful evaluation product.

In addition to surface-$f\mathrm{CO_2}$, we use dissolved inorganic carbon (DIC) concentrations within the ETPO measured during World Ocean Circulation Experiment cruise (WOCE) P19 in 1993 (Fig. 1; WOCE data available from http://cchdo.ucsd.edu/), and weekly dry-air CO2 mole fractions ($x\mathrm{CO_2}$) measured at Fanning Island (3.5° N, 159° W; as part of the Scripps $\mathrm{CO_2}$ program, http://scrippsco2.ucsd.edu/). We derive $f\mathrm{CO_2}$ in the atmosphere according to

$$f\mathrm{CO_2}_{\,\mathrm{air}} = x\mathrm{CO_2}(p_{\mathrm{atm}} - p_{\mathrm{H_2O}}), \tag{1}$$

where P_{atm} is the atmospheric pressure taken from the ERA-Interim product (http://www.ecmwf.int/en/research/climate-reanalysis/era-interim) and $p_{\mathrm{H_2O}}$, the saturated water pressure (Weiss, 1974).

2.2 Calculating air–sea fluxes of $\mathrm{CO_2}$

The air–sea flux of $\mathrm{CO_2}$ ($\mathrm{mmol\,m^{-2}\,d^{-1}}$) is derived using the difference between surface ocean and atmospheric $f\mathrm{CO_2}$ values, the solubility of $\mathrm{CO_2}$ in standard seawater ($\alpha\mathrm{CO_2}$ calculated using the values given by Weiss, 1974) and the gas transfer velocity $k\mathrm{CO_2}$ ($\mathrm{cm\,h^{-1}}$):

$$F = k\mathrm{CO_2}\,\alpha\mathrm{CO_2}(f\mathrm{CO_2}_{\,\mathrm{sea}} - f\mathrm{CO_2}_{\,\mathrm{air}}). \tag{2}$$

k is calculated using the 10 m wind-speed-based parameterisation described by Sweeney et al. (2007), where

$$k = 0.27U^2(660/Sc)^{0.5}, \tag{3}$$

where Sc is the Schmidt number for $\mathrm{CO_2}$ (Wanninkhof, 1992). We use the 0.25° daily resolution 10 m wind speed product from the Advanced Scatterometer (ASCAT; www.

knmi.nl/scatterometer/) to calculate air $f\mathrm{CO_2}$, assuming water vapour saturation at the boundary layer, then using the description in Eq. (1).

We note that when calculating air–sea gas exchange, it is not practical to derive a unique k parameter for all oceanic conditions and locations of interest, therefore, through necessity, k is calculated using the non-specific parametrisation of Sweeney et al. (2007). Influences on k, such as rainfall, have been observed to enhance gas transfer velocities in laboratory experiments (Liss and Johnson, 2014). However, applying the results from these laboratory experiments into a modified gas transfer velocity within the ETPO region is challenging, and requires further field experiments to be validated. It is for this reason, and the role that rainfall has in reducing DIC, (thus bringing $\Delta f\mathrm{CO_2}$ closer to atmospheric equilibrium and limiting the influence on air–sea fluxes brought about by an enhanced gas transfer velocity), we do not attempt to correct for the influence that rainfall has on air–sea exchanges.

2.3 Satellite observations of SST and SSS

Sea surface temperatures have been continuously measured from space via satellites since the AVHRR mission in 1981, and sea surface salinity has been measured since the launch of the European Space Agency's Soil Moisture and Ocean Salinity (SMOS) satellite mission in November 2009 (Kerr et al., 2010). In this paper, we use satellite temperature (T) and salinity (S)data to help in the interpretation of spatial variability of $f\mathrm{CO_2}$ from the ETPO.

SMOS SSS maps at 0.25° resolution (running average over $100 \times 100\,\mathrm{km^2}$) produced by the LOCEAN SMOS group (combining SMOS ascending and descending passes) were used within this paper (Boutin et al., 2013, data available at catds.ifremer.fr/Products/Available-products-from-CEC-OS/Locean-v2013). SMOS SSS data are not used prior to June 2010 due to variations in sensor configuration tested during the in-orbit sensor commissioning phase (Corbella et al., 2011). Analysing the accuracy of the SMOS product, using in situ point observations of SSS, can be completed using both SOCAT SSS data (where the salinity is derived from ship-mounted thermosalinograph – TSG), and Argo profiles made within the region (Appendix Fig. A1). Binning all Argo and TSG near-surface salinity data (that overlap the SMOS observational period) into the same monthly, 0.25° structure as the SMOS monthly 0.25° product, enables direct comparison. It is found that the RMSE between SMOS and these binned in situ data is 0.24 psu, with a minimal offset (of 0.04 psu, S; Fig. 1). This variability is a function of both the intrinsic variability of SSS within the EPTO (for example, caused by localised rainfall, riverine outflow, upwelling events that may occur within each SMOS observational pixel), and a measurement error made in the SMOS data. Estimates of this intrinsic variability within the tropics is 0.1 psu, but in certain regions (such as the western Pacific warm pool and the ETPO) may fea-
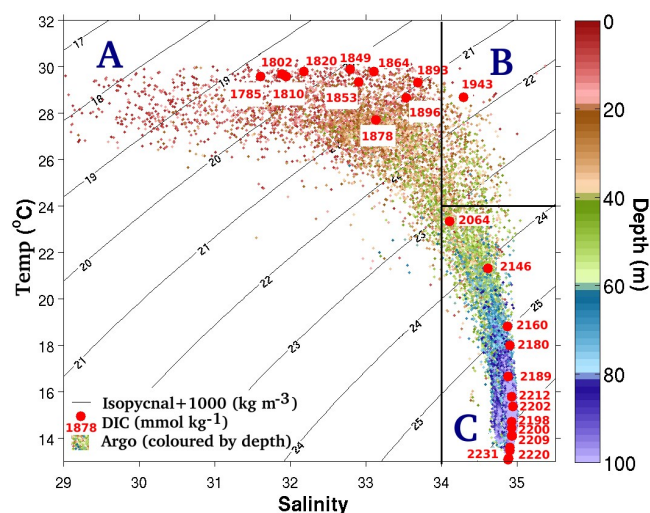
Figure 2. The total library of Argo profiles collected within the ETPO in the upper $100\,\text{m}$. Numbered red dots indicate the total dissolved carbon concentration at specific TS values as measured during the WOCE cruise P19.

ture variabilities of $0.4\,\text{psu}$ or higher (Delcroix et al., 2005). If the average intrinsic variability for the tropical Pacific (of $0.1\,\text{psu}$) is used, the measurement noise within the SMOS product is $0.14\,\text{psu}$. This measurement noise is included in our $f\text{CO}_2$ error estimates (as detailed below). We suggest that this is a satisfactory noise to signal ratio, given that the region features SSS variability of up to $8\,\text{psu}$ (Fig. 2).

SSS was combined with sea surface temperatures from the Operational Sea Surface Temperature and Sea Ice Analysis (OSTIA) system; an optimal interpolation of multiple microwave and infrared satellite-based data sources (Donlon et al., 2012). This SST daily product features a native resolution of $0.05°$, which was subsequently re-sampled over the same spatial and temporal grid as the SMOS data. As auxiliary data sets for near-surface T and S, data from the Argo float array were used.

2.4 The basis of using a SST/SSS statistical $f\text{CO}_2$ model in the ETPO

Using an $f\text{CO}_2$ model based on surface T and S properties requires the carbon properties of water masses to be quantified. We define three surface water masses within the study region, based on the near-surface (0–$100\,\text{m}$ depth) T and S characteristics of the ETPO recorded by ~ 6000 Argo profiles between 17 and $4°$ N, and east of $95°$ W (Fig. 2). These water masses are also independently featured within studies by Kessler (2002, 2006):

1. an ETPO surface water, with temperatures $> 27°$ C and salinities > 33.5 (Fig. 2, "B");

2. deep water that predominantly exists below the thermocline (defined by Kessler as the $20\,°\text{C}$ isotherm) and is

only expressed at the surface of the ETPO during periods of upwelling (Fig. 2, "C");

3. rain-influenced water, with salinities < 33.5 (Fig. 2, "A").

Here, the water mass at C (herein referred to as "deep water") is predominantly found at depths greater than $80\,\text{m}$, whilst the near-surface water is typically ETPO surface water and is warmer than $27.5\,°\text{C}$ (A and B). Occasionally, the deep water mass can be observed at shallower depths, advected upwards during times of strong upwelling (Fig. 2). Rainfall-influenced waters display a wide range of salinities (from 29 to 34.5) within the upper $20\,\text{m}$ (as observed in the salinity variation between A and B). At low salinities, densities as low as $1018\,\text{kg}\,\text{m}^{-3}$ are observed – an $8\,\text{kg}\,\text{m}^{-3}$ difference between this surface water and deep water (featuring densities of $1026\,\text{kg}\,\text{m}^3$). This large density gradient is an important feature of the ETPO, because in periods when stratification and high thermocline strengths are prevalent the upwelling of deep water is inhibited (Fiedler and Talley, 2006).

To identify the carbon properties of these water masses, DIC concentrations between the surface and $100\,\text{m}$ depth within the ETPO measured during the transect of WOCE P19 are shown as red circles and associated concentrations plotted within TS space (Fig. 2). Deep water (C) was observed to have DIC concentrations $> 2200\,\mu\text{mol}\,\text{kg}^{-1}$ and contrasting values between A and B of $< 1950\,\mu\text{mol}\,\text{kg}^{-1}$. End-member mixing occurs at intermediate temperatures between the two water masses B and C, exhibited in the gradient observed along the 34.2–34.75 isohalines in Fig. 2. Assuming that upwelling results in the expression of deep water at the surface, upwelling will act to increase the surface inventory of DIC, leading to increased $f\text{CO}_2$.

Rainfall results in surface layer dilution, thus reducing DIC between A and B (Turk et al., 2010). When the $f\text{CO}_2$ of both end members in this system (rainwater and surface waters) are at equilibrium with the atmosphere, this dilution results in a lowering of $f\text{CO}_2$ within the sea surface, and ingassing of CO_2. Turk et al.'s (2010) study in the western Pacific warm pool indicated that decreases of 30–40 μatm in surface-$f\text{CO}_2$ values can result from rainfall alone, with these effects strongest under highly stratified conditions. This suggests that rainfall could be an important influence on ETPO $f\text{CO}_2$, particularly within the rainfall-dominated Panama Basin region. Finally, although biological processes influence DIC (and hence $f\text{CO}_2$), observations of DIC within this region suggest that physical processes (such as upwelling or rainfall) are the first-order control on DIC. For this reason, coupled to the lack of net community production data within the region, we have elected to concentrate our efforts on quantifying these physical processes.

2.5 Processing SOCAT data

Surface $f\mathrm{CO_2}$ responds to changing levels of atmospheric $f\mathrm{CO_2}$, which is increasing at approximately $20\,\mu\mathrm{atm}$ per decade, (Takahashi et al., 2009, Fig. 3). In order to calculate contemporary air–sea fluxes, the multi-year SOCAT data must first be temporally corrected for the interannual trend of increasing atmospheric $\mathrm{CO_2}$. The mean annual increase in $f\mathrm{CO_2}$ within the central equatorial Pacific ($5°\,\mathrm{N}$ and $5°\,\mathrm{S}$) between 1979 and 1990 (excluding El Niño events) was estimated at a rate of $1.1\,\mu\mathrm{atm} \pm 0.3$ per year (Takahashi et al., 2009). A second estimate, using data collected between 1990 and 2003 (within the region $10°\,\mathrm{N}$ to $5°\,\mathrm{S}$) calculated an annual increase of $2.0\,\mu\mathrm{atm} \pm 0.2$ (Takahashi et al., 2009). Correcting 1991 data to contemporary July 2014 values would equate to a not-inconsiderable difference, depending on which of these two estimates was chosen. Therefore, in order to choose the optimum correction for the smaller subregion of the ETPO, all available SOCAT $f\mathrm{CO_2}$ data 1991–2011 were binned by year the data were collected (Fig. 3). Fitting a linear regression to the average bin value of this data resulted in an average annual increase of $1.95\,\mu\mathrm{atm\,yr^{-1}}$ ($\pm 0.38\,\mu\mathrm{atm}$). This linear regression was found to fall within the 5th and 95th percentile values for all bins, with variability in mean and median values caused by heterogeneous sampling of the region and interannual variability (Fig. 3, percentiles plotted in blue). Our calculated rate of increase is within the range of the annual atmospheric $f\mathrm{CO_2}$ increase measured at Fanning Island ($1.8\,\mu\mathrm{atm\,yr^{-1}} \pm 0.1\,\mu\mathrm{atm}$), suggesting that $f\mathrm{CO_2}$ within the ETPO tracks the rate of increasing atmospheric $f\mathrm{CO_2}$ (Fig. 3). Therefore, we apply a $1.95\,\mu\mathrm{atm}$ per year correction to the SOCAT data in order to normalise the $f\mathrm{CO_2}$ data to 1 July 2014 values, with all results herein also normalised to this date.

Although the spatial distribution of $f\mathrm{CO_2}$ SOCAT observations within the ETPO is irregular, the variability can be constrained once the TS properties of the surface ocean are accounted for (as per DIC, Figs. 2, 4). Data from the upper $100\,\mathrm{m}$ of Argo profiles completed in each of the three gulfs (Panama, Papagayo and Tehuantepec, as defined in Fig. 1) show strong TS similarities between each of the three gulf regions; low-salinity (< 34) waters are observed in each gulf, with a thermocline separating surface water and deep water at 80–$100\,\mathrm{m}$ depth. The TS properties of these Argo profiles are replicated at the surface, within SOCAT SST and SSS data (Fig. 4). However, the relative number of observations that fall into each water mass definition is different. The warm ETPO surface water is dominant in all three regions for the majority of samples, but cooler ($< 20\,°\mathrm{C}$) deep water is occasionally expressed at the surface, with this signal strongest in the Gulf of Tehuantepec, followed by the Gulf of Papagayo and seldom observed in the Gulf of Panama. This contrasts observations of low-salinity water, which are very frequent within the Gulf of Panama, but rare in the other two gulfs (Fig. 4). Although both SOCAT and Argo data suffer
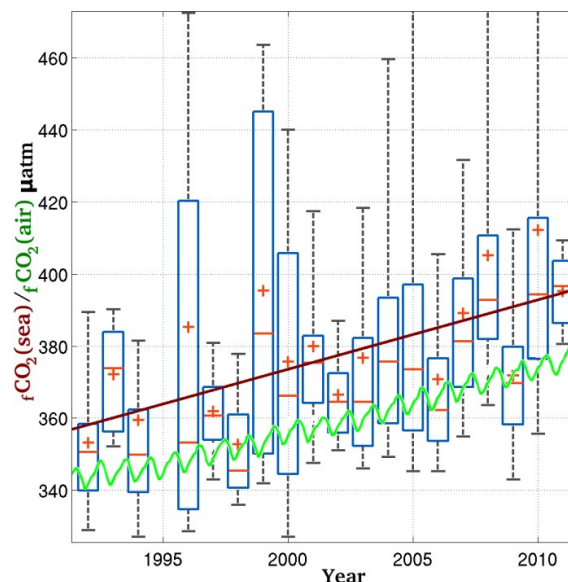

Figure 3. Yearly binned $f\mathrm{CO_2}$ measurements from the SOCAT database. The interpolated average rate of ETPO $f\mathrm{CO_2}$ increase is shown as a red line, with the atmospheric $f\mathrm{CO_2}$ data shown as a green line. The blue boxes represent the 5th and 95th percentile $f\mathrm{CO_2}$, with the small red lines indicating yearly averages, and the red crosses indicating the yearly median.

from sparse sampling, we suggest that both data sets indicate that the relative dominance of each water mass within each of the three gulfs is different. There are very few SOCAT observations within the offshore (OS) region (Fig. 1), thus we do not show a TS diagram from this region; however, Argo profiles from this region are included in Fig. 2, highlighting that the OS also shares the same water masses as the three gulf regions.

The distribution of DIC concentrations within TS space is mirrored by $f\mathrm{CO_2}$ values; deep water features higher $f\mathrm{CO_2}$ values than ETPO surface water, and low-salinity water features the lowest $f\mathrm{CO_2}$ values. The intermediate values of $f\mathrm{CO_2}$ observed between each of these water masses suggest end-member mixing of $f\mathrm{CO_2}$ between water masses. Finally, there are no water masses that share TS characteristics, but feature very different DIC concentrations or $f\mathrm{CO_2}$ values, meaning that DIC/$f\mathrm{CO_2}$ values are unique within TS space in this region (Figs. 2 and 4). Therefore, as both DIC and $f\mathrm{CO_2}$ values behave pseudo-conservatively within TS space, it is possible to construct a statistical description of $f\mathrm{CO_2}$ using solely SSS and SST.

2.6 Fitting a statistical description – the look-up table

The similarities of T, S and $f\mathrm{CO_2}$ properties of the water masses observed both by Argo and within the SOCAT database across all three gulfs enable data from the entire ETPO to be considered as a single system (Fig. 5a). As the
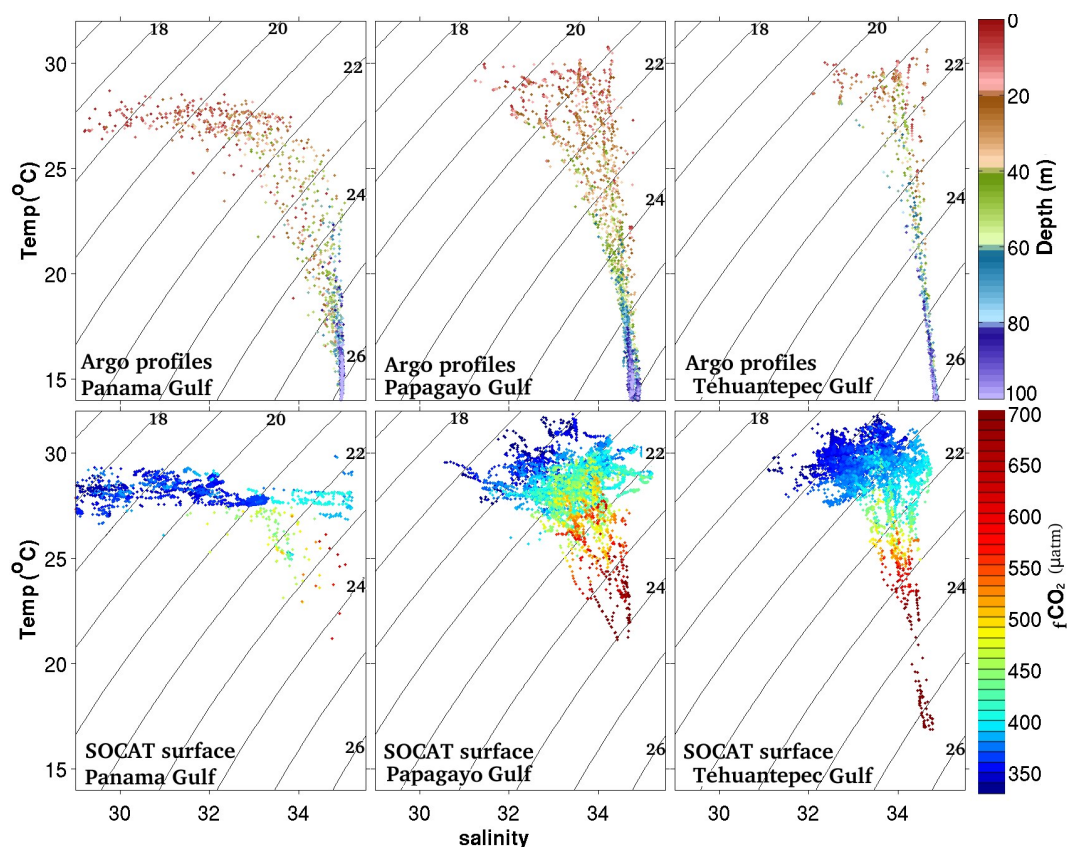
Figure 4. TS data from the three main gulfs within the ETPO both from Argo floats (coloured according to depth – top three plots) and from surface SOCAT T and S data, (coloured according to level of $f\mathrm{CO}_2$ – bottom three plots.

variance between individual $f\mathrm{CO}_2$ observations occupying the same location within TS space is low (Fig. 5b) we use a look-up table (LUT) to describe $f\mathrm{CO}_2$ as a function of T and S. This LUT technique, although not previously used to estimate oceanic $f\mathrm{CO}_2$, has proven useful for estimating net primary productivity using satellite observations (Zhao et al., 2005). The LUT in this study uses a mesh of equal sized bins within T-S space. Observations of $f\mathrm{CO}_2$ within these discrete TS bins are collected, and an average $f\mathrm{CO}_2$ within TS space calculated. As each bin is fully independent of neighbouring bins, non-linear and/or skewed $f\mathrm{CO}_2$ distributions within TS space – and hence an improved synthetic $f\mathrm{CO2}$ product – can be accounted for with a lower attained root-mean-square error (RMSE) compared to using an alternative linear statistical description, such as a basic linear fit.

By combining all SOCAT data from the ETPO onto a single T-S diagram, a look-up table (LUT) can be produced in order to describe $f\mathrm{CO}_2$ as a function of T and S (Fig. 5). The LUT was constructed by completing a linear interpolation of binned 0.1 (salinity) $\times$ 0.1 °C SOCAT data from the entire ETPO region. The number of observations per bin is depicted in the right-hand panel. Here the highest number of observations fall in a narrow region of TS space, between

salinities of 32–34.5 and 25–30 °C (Fig. 5). We tested the quality of fit of the SOCAT-based LUT, using LDEO v2013 data. Here $f\mathrm{CO}_2$ values were computed using the LUT and using T and S from the LDEO v2013 database, with these computed $f\mathrm{CO}_2$ data compared to the measured (annual-increase-corrected) $f\mathrm{CO}_2$ values. The LUT could be applied to 96.2 % of all LDEO v2013 T-S measurements made between 1990 and 2013, with the remaining TS measurements falling outside the TS boundaries of the LUT.

The average root-mean-square error (RMSE) of the LUT was 16.8 µatm between the LUT computed and measured $f\mathrm{CO}_2$. This RMSE was asymmetrically distributed; it was highest at temperatures of 22–26 °C/salinities of 34.4, and lowest at warmer temperatures/lower salinities and also at colder temperatures (Fig. 5). This suggests that $f\mathrm{CO}_2$ variability is low in aged surface waters, and high in recently upwelled and warming water. As there are a number of measurements within the region of higher error (Fig. 5), we hypothesise that this larger uncertainty is not due to lack of observations, but rather to mixing/heating processes that allow water with slightly different $f\mathrm{CO}_2$ values to occupy the same TS space. For example, the $f\mathrm{CO}_2$ value of water at salinities of 34.5 and 25 °C could either result from the stoichiometric
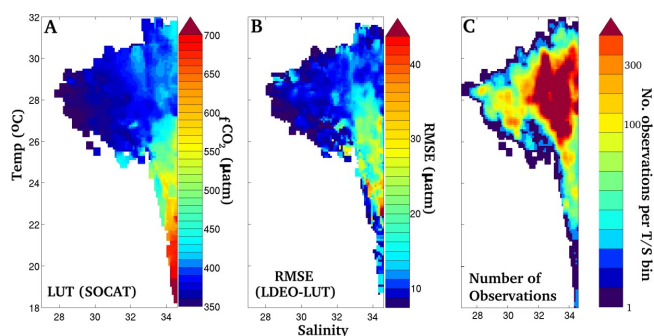
Figure 5. (a) The look-up table derived from the position of ETPO SOCAT $f\mathrm{CO_2}$ measurements within TS space. **(b)** The root-mean-square error of the LUT–$f\mathrm{CO_2}$ observations, showing the variance between $f\mathrm{CO_2}$ observed within the same TS space in the LUT. **(c)** The number of LDEO measurements per $0.1° \times 0.1°$ salinity/temperature bins that went into generating the LUT.

mixing of two waters at salinities of 34.5, and temperatures of 18 and 32 °C, or solely from warmed 34.5/18 °C water. The $f\mathrm{CO_2}$ observed within the ETPO result from the influences of upwelling, solar radiation, horizontal advection, biological productivity and diapycnal mixing. Therefore it is impossible to define a perfect relationship between the physical attributes of the water and resulting $f\mathrm{CO_2}$ concentration. However, this LUT technique works efficiently in determining the first-order variability of the system within the ETPO. In order to calculate the uncertainty of these LUT-derived synthetic $f\mathrm{CO_2}$ data, we complete the mean-square error calculation based on the variance of $f\mathrm{CO_2}$ data within each cell of the LUT and the uncertainty of SMOS SSS (as described above.) We assume that the SST and SSS measurements within SOCAT and the OSTIA SST product are accurate. This error is propagated through the air–sea flux estimates in order to calculate the error of the air–sea flux values (as reported in Table 1).

3 Results

3.1 Bimonthly variability along ship paths

Bimonthly $f\mathrm{CO_2}$ variability can be seen in the (1991–2011 annual-$f\mathrm{CO_2}$-increase-corrected) SOCAT observations plotted in Fig. 6. Here, the top six panels display SOCAT observations of $f\mathrm{CO_2}$, and the lower six panels display $f\mathrm{CO_2}$ calculated from SOCAT SST and SSS observations using the LUT. As the majority of SOCAT data are collected using ships of opportunity, resolution within shipping lanes in the ETPO is excellent; for example, multiple observations are made in regions south and west of the Panama Canal, at 9.1° N, 79.7° W, but are very sparse outside of these shipping lanes. However, though these issues in data resolution are acknowledged, patterns in $f\mathrm{CO_2}$ can still be detected. The lowest $f\mathrm{CO_2}$ is typically observed within the Gulf of Panama

and close to the coast. Higher $f\mathrm{CO_2}$ is observed in the gulfs of Tehuantepec and Papagayo. Interseasonal variability is also observed, with the highest $f\mathrm{CO_2}$ ($> 440\,\mu\mathrm{atm}$) occurring between November and February, with lower $f\mathrm{CO_2}$ values ($< 400\,\mu\mathrm{atm}$) occurring across the entire region during the summer months (May–August). The data also show a very high degree of variability at small spatial and temporal scales, for example during November–December within the Gulf of Papagayo. It is this variability that needs to be resolved using the LUT, when coupled to satellite SST and SSS observations at native resolution. Thus, it is important to confirm that the LUT is able to recreate this variability in $f\mathrm{CO_2}$ using the initial (SOCAT) T and S conditions. Here, we find that the LUT performs well, with most of the measured $f\mathrm{CO_2}$ variability also observed within the $f\mathrm{CO_2}$ calculated using the LUT (Fig. 6).

3.2 $f\mathrm{CO_2}$ and fluxes by region – the influence of wind and upwelling

Using the LUT, SMOS and OSTIA data, the small-scale variability and features within the ETPO can be resolved more thoroughly than is possible through SOCAT data alone. Bimonthly averaged (between July 2010 and June 2014) SSS, SST, $f\mathrm{CO_2}$, $\mathrm{CO_2}$ flux and wind speed are plotted in Fig. 7. Jet wind velocities over the Gulf of Tehuantepec are at their peak between October and February, thus optimising Ekman upwelling. During these months the SSS of the gulf increases, whilst the SST decreases (due to the influences of upwelling). Increased $f\mathrm{CO_2}$ is observed across most of the Gulf of Tehuantepec, with peak outgassing occurring as a narrow band, centred underneath the axis of the jet wind. We suggest that this is due to the complimentary nature of ocean physics in this region – high wind speeds promote Ekman upwelling of high DIC deep water, whilst increasing the k component within the air–sea flux parameterisation, thereby maximising $\mathrm{CO_2}$ outgassing.

4 Discussion

The Gulf of Papagayo shares many similarities with the Gulf of Tehuantepec; however, jet winds are more zonally aligned (reducing Ekman pumping strengths; Alexander et al., 2012), and occur later in winter compared to Tehuantepec, being strongest between November and February. This results in a lag between peak wintertime $f\mathrm{CO_2}$ values seen within the two gulfs (Figs. 7 and 8). The Gulf of Papagayo also features elevated $f\mathrm{CO_2}$ values during the summer months which are not seen in either the Gulf of Tehuantepec or Panama. This is due to westerly winds maintaining the vorticity of the Costa Rican dome structure, enabling the continued upwelling of deep water at the core of this dome throughout the summer season (Grodsky et al., 2014, Kessler, 2006, Fig. 7).
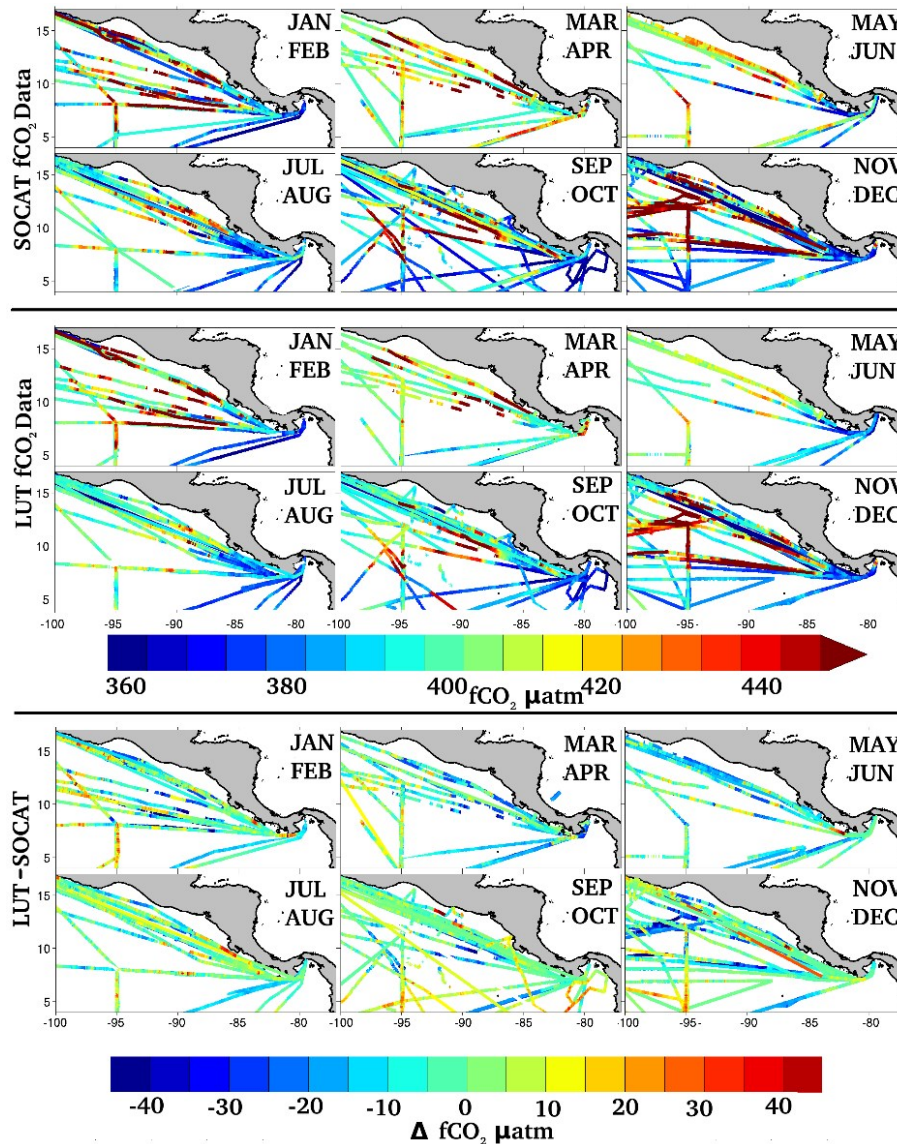
Figure 6. SOCAT fCO$_2$ bimonthly (January+February, March+April, May+June, July+August, September+October, November+December) observations within the ETPO corrected for the annual CO$_2$ increase, LUT-derived bimonthly fCO$_2$ calculated using SOCAT SST and SSS observations and LUT SOCAT observations.

The seasonally averaged wind velocities in the Gulf of Panama superficially resemble the wind patterns in the two northern gulfs – jet winds are observed between January and February (Fig. 7). However, excluding a small area of ocean directly underneath the wind jet axis during winter, the region remains a small net sink of carbon throughout the year (Fig. 8). We suggest that this contrast between the Gulf of Panama and the rest of the ETPO is due to the high rainfall within this region, resulting in the dilution of DIC as described above.

4.1 fCO$_2$ and the influence of rainfall

A significant proportion of atmospheric water exported from above the Atlantic basin into the Pacific basin is precipitated into the ETPO. This rainfall is intensified within the ETPO during the summertime, due to a northwards shift of the ITCZ towards the Panama coast (Xie et al., 2005). As a result, the Gulf of Panama receives net precipitation of 180–220 cm per year, with peak rainfall of 20 mm per day during July–August (Alory et al., 2012). This large freshwater flux, coupled with light southerly winds between March and June, and the southerly (thus promoting downwelling) winds between July and December, results in the semi-permanent
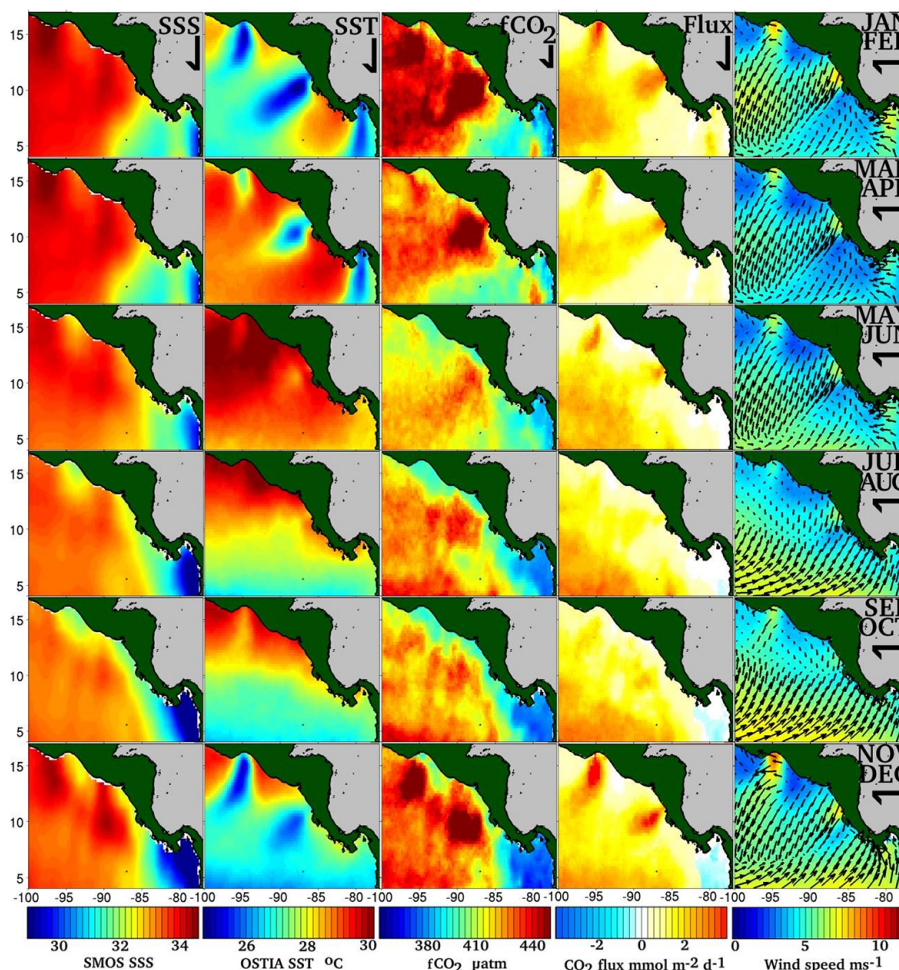
Figure 7. July 2010–June 2014 average SSS, SST, LUT-derived $f\mathrm{CO}$, air–sea fluxes and wind vectors for the ETPO, split bimonthly (January+February, March+April, May+June, July+August, September+October, November+December).

stratification of the water column (Fig. 7, Alory et al., 2012). Qualitatively, this stratification can be observed in the SO-CAT and Argo data in Fig. 4 by the scarcity of deep water observations in the Gulf of Panama compared to the gulfs of Tehuantepec and Papagayo. Additionally, the thermocline is observed at deeper depths in the Argo profiles taken in the Gulf of Panama, compared to either the Gulf of Tehuantepec or Papagayo (Fig. 4).

The influence of stratification/rainfall on $f\mathrm{CO_2}$ values is seen in Fig. 7. Here, the lowest salinity and $f\mathrm{CO_2}$ are observed during the summer months (during peak rainfall season; Alory et al., 2012). This low-$f\mathrm{CO_2}$, stratified system persists until January, when intensification of the South Equatorial Current results in the export of the low-$f\mathrm{CO_2}$/fresh surface layer towards the southwest (as seen by the elongation of the fresh pool during January–March SSS). This export of water, coupled with the dry season within the Gulf of Panama, appears to weaken the stratification, with the result that sporadic jet winds enable Ekman upwelling,

thus increasing SSS (Alory et al., 2012, Fig. 7) and average $f\mathrm{CO_2}$ values between January and April (Fig. 8).

4.2 Air–sea fluxes from July 2010 to June 2014

The ETPO between 2010 and June 2014 had an annual average $\Delta f\mathrm{CO_2}$ 39.4 µatm ($\pm$10.7) and a outgassing $\mathrm{CO_2}$ flux of 1.51 mmol m^{-2} d^{-1} ($\pm$0.41; Fig. 8/Table 1). The ETPO (the boundaries of which defined as per Fig. 1) has an area of 1.9×10^{12} m^2, therefore net outgassing from the ETPO equates to 10×10^{12} g (0.01 Pg) of carbon per year.

To examine both monthly and interannual variability in air–sea fluxes, the ETPO is split into subregions: the gulfs of Tehuantepec, Papagayo, Panama and the offshore region (Figs. 1, 8 and Table 1). Here, although it is variable, the consistent seasonal cycle between summer and winter observed in the bimonthly data in Fig. 7 is present for each individual year. Peak outgassing within the gulfs of Tehuantepec, Papagayo and the South Equatorial Current occurs during winter (November–February). This contrasts with the Gulf of
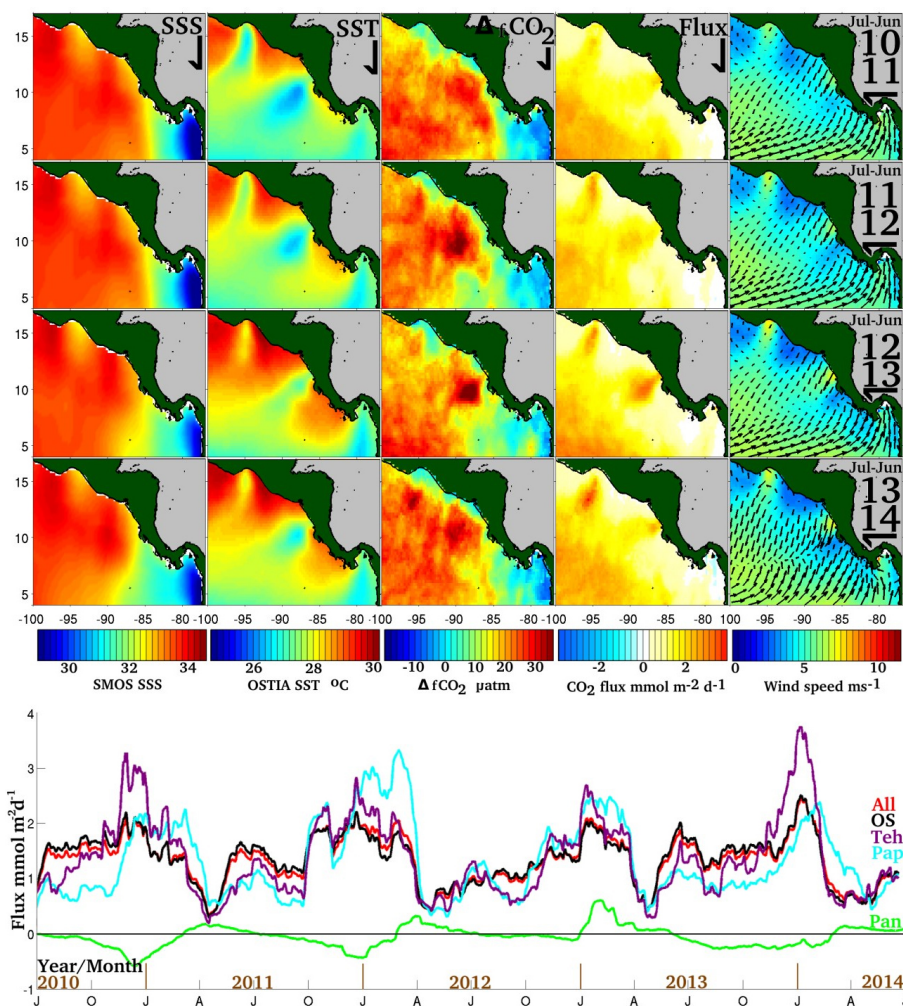
Figure 8. Upper image: yearly average SSS, SST LUT-derived ΔfCO$_2$, air–sea fluxes and wind vectors for the ETPO for July to June 2010+2011, 2011+2012, 2012+2013 and 2013+2014. Lower image: the continuous LUT-derived fCO$_2$ fluxes from the entire ETPO (red line), the gulfs of Tehuantepec (purple), Papagayo (blue), Panama (green) and the South Equatorial Current (black).

Panama, which is a net sink of atmospheric CO$_2$ except during occasional upwelling events during January–February. However, ingassing within the Gulf of Panama is insufficient to offset outgassing from the rest of the ETPO, and the region remains a net source of CO$_2$ year round.

In addition to seasonal variability, interannual variability is observed within the ETPO. Across the entire basin, the ETPO during the years 2010–2012 were on average cooler and saltier than subsequent years (especially 2012–13). This resulted in higher annually averaged outgassing and fCO$_2$ values (Fig. 8, Table 1). Concurrently, during 2010–2012, the Gulf of Panama featured a low-salinity mimima (of 28), and a small fresh pool footprint (the boundary of which is defined by the 33 isohaline; Alory et al., 2012). The extreme low salinity observed within the eastern region of the Gulf of Panama during 2010 to 2012 resulted in lower fCO$_2$ and hence stronger ingassing than 2012–2014 values, highlight-

ing the effect of rainwater dilution of DIC. However, this localised ingassing was insufficient to offset the higher outgassing observed in the other regions of the ETPO (Fig. 8, Table 1). Also noteworthy is that average wind velocities were similar during 2010 and 2012 compared to subsequent years, so the increased outgassing observed during these years cannot be attributed to increased wind-mediated Ekman upwelling of deep water alone.

We note that the period of 2010 to the end of 2011 featured La Niña conditions, and suggest that this could be causal to the differences in CO$_2$ fluxes, higher salinities and higher fCO$_2$ observed during this time period. A study using NCEP (National Centers for Environmental Prediction) reanalysis data within this region observed cooler waters and more frequent upwelling of sub-thermocline deep water during La Niña events. A shallower thermocline depth exists during La Niña events, which results from the uplift of the water col-

umn by intensified coastal Kelvin waves. Mechanistically, this shallow thermocline reduces the strength of upwelling required for the expression of deep water at the surface, thus decreasing average SSTs observed during La Niña periods (Alexander et al., 2012).

Furthermore, a study by Alexander et al. (2012) also suggests that although jet winds are the first-order control on SST and thermocline depth during winter, it is changes in the thermocline depth (rather than changes in jet winds) that result in observed El Niño–Southern Oscillation (ENSO) variability in SST within the ETPO. Variability in thermocline depth, and by association, variability in the ease by which deep water can be advected towards the surface, suggests that the ENSO could drive variability within the surface-$f\mathrm{CO}_2$ observations. However, with only 4 years of data, and no El Niño phase for intercomparison, we are unable to draw definitive conclusions.

4.3 Previous work

The results in Figs. 7 and 8 represent the first attempt to quantify $f\mathrm{CO}_2$ within the ETPO region at high resolution using observations. Previous work encompassing the ETPO includes three basin-wide or global $f\mathrm{CO}_2/p\mathrm{CO}_2$ studies, by Takahashi et al. (2009), Ischii et al. (2014) and Landschützer et al. (2014). These studies, as discussed in the introduction, are based on the extrapolation of $p\mathrm{CO}_2$ directly, or the extrapolation of $p\mathrm{CO}_2$ using a neural network technique, and feature spatial resolutions of $4° \times 5°$, $4° \times 5°$ and $1° \times 1°$ respectively. Of these three studies, only the study by Takahashi et al. (2009) features a data set of calculated $\Delta p\mathrm{CO}_2$ that includes the ETPO region, thus allowing direct comparison with our calculations. Collocating the $\Delta p\mathrm{CO}_2$ results from Takahashi et al. (2009) within the ETPO regions defined in Fig. 1, the gulfs of Tehuantepec, Papagayo, Panama and the offshore region featured values of $+28.9$, $+54.1$, $+17.1$ and $+19.5\,\mu\mathrm{atm}$ respectively (Table. 1). This suggests that the Takahashi et al. (2009) study differentiates the low $\Delta p\mathrm{CO}_2$ Gulf of Panama region from the higher values observed in the gulfs of Tehuantepec and Papagayo. The resolution used in Takahashi's study is too coarse to identify any mesoscale features (such as upwelling), or interannual variability within the region. However, we find that an average $\Delta p\mathrm{CO}_2$ value from Takahashi et al. (2009) of 29.1 μatm was within the error limits of this study (Table 1).

Applying the same wind speed product and gas transfer parametrisation used in this study to the ETPO $\Delta p\mathrm{CO}_2$ values from Takahashi et al. (2009), we find that all regions are outgassing, with the Gulf of Papagayo dominant within the ETPO (Table 1). The ingassing observed within the Gulf of Panama for our study is not replicated in Takahashi et al. (2009). The improved resolutions featured in Landschützer et al. (2014) resulted in some mesoscale features being observed, such as the increased $p\mathrm{CO}_2$ values within the Gulf of Papagayo. However, this work was not able to identify the low $p\mathrm{CO}_2$ conditions within the Gulf of Panama, most likely due to the same biogeochemical province description being applied to the entire ETPO. In addition to these studies, our work distinguishes the importance of jet winds in increasing $p\mathrm{CO}_2$, and quantifies the strong interannual variability within the region.

5 Conclusions

Estimating surface-$f\mathrm{CO}_2$ and air–sea fluxes of CO_2 within the global oceans has advanced considerably over the past decade, assisted by the assembly of large standardised atlases of surface observations (such as the SOCAT database). However, although these databases boast measurements in the millions, a challenge remains in gauging seasonal or sub-mesoscale $f\mathrm{CO}_2$ variability in the oceans. Sampling through the use of commercial volunteering observation vessels may introduce bias, with most data existing within the narrow confines of the major global shipping lanes or for only a few months of the year. However, the quantification of $f\mathrm{CO}_2$ within TS space, used in conjunction with observations of surface SST and SSS (made possible through the recent availability of SSS data from satellites), has proved highly useful in improving our understanding of $f\mathrm{CO}_2$ variability at much improved spatial and temporal resolutions. We have demonstrated a technique using SOCAT data to identify the $f\mathrm{CO}_2$ signatures of water masses within the ETPO region, namely, the high $f\mathrm{CO}_2$ deep water, the near-equilibrium ETPO surface water and the undersaturated rainfall diluted surface waters. From this, we used a LUT technique to produce a description of the $f\mathrm{CO}_2$ content of ETPO surface water using satellite SST and SSS data. The highest outgassing and surface-$f\mathrm{CO}_2$ values were observed during the winter period (November–March), in the gulfs of Tehuantepec, Papagayo and in the South Equatorial Current. The first-order control on these upwelling events, and hence $f\mathrm{CO}_2$ in the ETPO, are strong wind jets blowing through low-altitude gaps in the Central American cordillera. The Gulf of Panama remained undersaturated on average, due to dilution effects of heavy rainfall and the stratification of the water column. Although wind jets were observed in the Gulf of Panama, the exceptionally low density of the water within this region appears to limit upwelling, and any upwelling that occurs is directly underneath the wind jet axis. Inter-annual variability was observed within the region, with the location of the western extent of the fresh pool moving considerably westwards between 2010 and 2014. Previous work within this region suggests that changes in thermocline depth related to ENSO are likely to influence $f\mathrm{CO}_2$ within this region. The region is a net contributor to atmospheric CO_2, with average sea to air fluxes (over the 4 years of observations) of $1.5\,\mathrm{mmol\,m^{-2}\,d^{-1}}$, with all regions of the ETPO outgassing throughout the year, except the rainfall-diluted Gulf of Panama/fresh pool region.

Appendix A

Table A1. Annual averaged values for each region, as reported in Fig. 8, and average values from Takahashi et al. (2009).

| Date/location	$\Delta f\text{CO}_2$ (µatm)	CO_2 flux (mmol m^{-2} d^{-1})	CO_2 flux error ($\pm$mmol m^{-2} d^{-1})	Wind (ms^{-2})	Salinity	Temp (°C)
2010–2011 ETPO	40.4	1.55	0.39	4.81	33.3	27.9
2010–2011 Offshore (OS)	41.1	1.62	0.40	5.18	33.2	27.7
2010–2011 Panama (Pan)	−4.7	−0.19	−0.03	4.57	28.3	27.4
2010–2011 Papagayo (Pap)	34.8	0.95	0.20	4.17	33.7	28.2
2010–2011 Tehuantepec (Tec)	40	1.55	0.33	3.72	33.6	29.0
2011–2012 ETPO	42	1.56	0.43	4.59	33.3	27.9
2011–2012 OS	43.2	1.60	0.48	4.97	33.1	27.7
2011–2012 Panama	−4.1	−0.21	0.05	4.02	28.4	27.5
2011–2012 Papagayo	34.1	1.09	0.34	4.01	33.7	27.9
2011–2012 Tehuantepec	49.3	1.64	0.36	3.90	33.7	28.4
2012–2013 ETPO	35.3	1.41	0.40	4.88	33.2	28.6
2012–2013 OS	37.1	1.50	0.43	5.11	33.0	28.3
2012–2013 Panama	−2.1	−0.11	0.08	3.92	28.7	27.3
2012–2013 Papagayo	32.8	1.08	0.37	4.49	33.6	28.5
2012–2013 Tehuantepec	32.5	1.52	0.43	4.08	33.6	29.3
2013–2014 ETPO	39.9	1.53	0.41	4.67	33.3	28.0
2013–2014 OS	39.3	1.63	0.45	5.09	33.0	27.8
2013–2014 Panama	−2.8	−0.16	0.05	3.88	27.5	27.7
2013–2014 Papagayo	37.9	1.15	0.38	4.15	33.7	28.0
2013–2014 Tehuantepec	47.7	1.57	0.43	3.92	33.7	28.6
Average ETPO	39.4	1.51	0.41	4.7	33.3	28.10
Average OS	40.2	1.59	0.44	5.1	33.1	27.88
Average Panama	−3.4	−0.17	0.04	4.1	28.2	27.48
Average Papagayo	34.9	1.07	0.32	4.2	33.7	28.15
Average Tehuantepec	42.4	1.57	0.42	3.91	33.7	28.83
Takahashi 2009: ETPO	29.1	0.78	N/A	4.74	33.3	28.10
Takahashi 2009: OS	19.5	0.65	N/A	5.09	33.1	27.88
Takahashi 2009: Pan	17.1	0.54	N/A	4.10	28.2	27.48
Takahashi 2009: Pap	54.1	1.83	N/A	4.21	33.7	28.15
Takahashi 2009: Tec	28.9	0.71	N/A	3.91	33.7	28.83
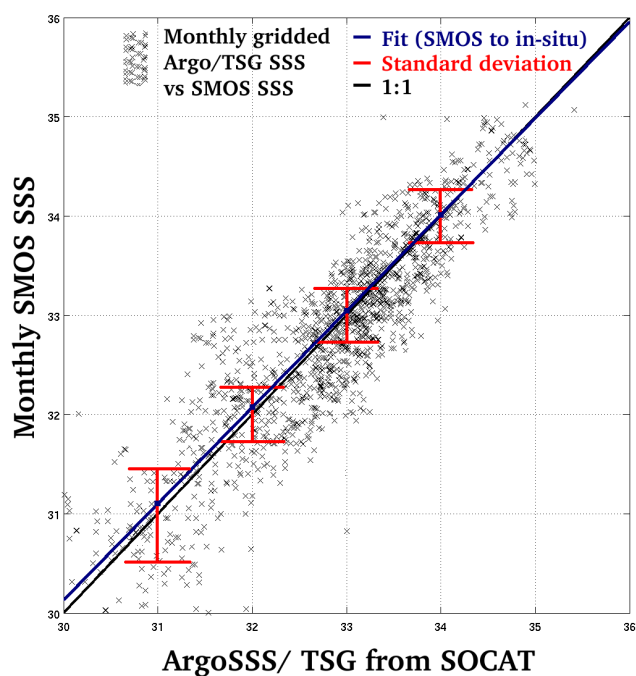
Figure A1. A comparison of in situ salinity measurements (from ship-mounted thermosalinograph or Argo) and corresponding SMOS salinity measurements made within the ETPO between July 2010 and December 2014. The fit and 1 : 1 relationships are indicated by the blue and black lines, and the error bars indicate the standard deviation between the two measurements for each 1 psu salinity bin.

References

Alexander, M. A., Seo, H., Xie, S. P., and Scott, J. D.: ENSO's Impact on the Gap Wind Regions of the Eastern Tropical Pacific Ocean, J. Clim., 25, 3549–3565, 2012.

Alory, G., Maes, C., Delcroix, T., Reul, N., and Illig, S.: Seasonal dynamics of sea surface salinity off Panama: The far Eastern Pacific Fresh Pool, J. Geophys. Res., 117, C04028, doi:10.1029/2011JC007802, 2012.

Bakker, D. C. E., Pfeil, B., Smith, K., Hankin, S., Olsen, A., Alin, S. R., Cosca, C., Harasawa, S., Kozyr, A., Nojiri, Y., O'Brien, K. M., Schuster, U., Telszewski, M., Tilbrook, B., Wada, C., Akl, J., Barbero, L., Bates, N. R., Boutin, J., Bozec, Y., Cai, W.-J., Castle, R. D., Chavez, F. P., Chen, L., Chierici, M., Currie, K., de Baar, H. J. W., Evans, W., Feely, R. A., Fransson, A., Gao, Z., Hales, B., Hardman-Mountford, N. J., Hoppema, M., Huang, W.-J., Hunt, C. W., Huss, B., Ichikawa, T., Johannessen, T., Jones, E. M., Jones, S. D., Jutterström, S., Kitidis, V., Körtzinger, A., Landschützer, P., Lauvset, S. K., Lefèvre, N., Manke, A. B., Mathis, J. T., Merlivat, L., Metzl, N., Murata, A., Newberger, T., Omar, A. M., Ono, T., Park, G.-H., Paterson, K., Pierrot, D., Ríos, A. F., Sabine, C. L., Saito, S., Salisbury, J., Sarma, V. V. S. S., Schlitzer, R., Sieger, R., Skjelvan, I., Steinhoff, T., Sullivan, K. F., Sun, H., Sutton, A. J., Suzuki, T., Sweeney, C., Takahashi, T., Tjiputra, J., Tsurushima, N., van Heuven, S. M. A. C., Vandemark, D., Vlahos, P., Wallace, D. W. R., Wanninkhof, R., and Watson, A. J.: An update to the Surface Ocean CO$_2$ Atlas (SOCAT version 2), Earth Syst. Sci. Data, 6, 69–90, doi:10.5194/essd-6-69-2014, 2014.

Boutin, J., Etcheto, J., and Dandonneau, Y.: Satellite sea surface temperature: a powerful tool for interpreting in situ $p\mathrm{CO}_2$ measurements in the equatorial Pacific Ocean, Tellus B, 51B, 490–508, 1999.

Boutin, J., Martin, N., Reverdin, G., Yin, X., and Gaillard, F.: Sea surface freshening inferred from SMOS and ARGO salinity: impact of rain, Ocean Science, 9, 183–192, doi:10.5194/os-9-183-2013, 2013.

Chelton, D. B., Esbensen, S. K., Schlax, M. G., Thum, N., Freilich, M. H., Wentz, F. J., and Schopf, P. S.: Observations of coupling between surface wind stress and sea surface temperature in the eastern tropical Pacific, J. Climate, 14, 1479–1498, 2001.

Corbella, I., Torres, F., Duffo, N., González-Gambau, V., Pablos, M., Duran, I., and MartínNeira, M.: MIRAS Calibration and Performance: Results From the SMOS In-Orbit Commissioning Phase, IEEE Trans. Geosci. Remote Sens., 49, 3147–3155, 2011.

Cosca, C. E., Feely, R. A., Boutin, J., Etcheto, J., McPhaden, M. J., Chavez, F. P., and Strutton, P. G.: Seasonal and interannual CO$_2$ fluxes for the central and eastern equatorial Pacific Ocean as determined from $f\mathrm{CO}_2$-SST relationships, J. Geophys. Res.-Oceans, 108, 3278, doi:10.1029/2000JC000677, 2003.

Delcroix, T., McPhaden, M. J., Dessier, A., and Gouriou, Y.: Time and space scales for sea surface salinity in the tropical oceans, Deep-Sea Res. Pt. I, 52, 787–813, doi:10.1016/j.dsr.2004.11.012, 2005.

Donlon, C. J., Martin, M., Stark, J., Roberts-Jones, J., Fiedler, E., and Wimmer, W.: The operational sea surface temperature and sea ice analysis (OSTIA) system, Remote Sens. Environ., 116, 140–158, 2012.

Feely, R. A., Takahashi, T., Wanninkhof, R., McPhaden, M. J., Cosca, C. E., Sutherland, S. C., and Carr, M. E.: Decadal variability of the air-sea CO$_2$ fluxes in the equatorial Pacific Ocean, J. Geophys. Res.-Oceans, 111, doi:10.1029/2005JC003129, 2006.

Fiedler, P. C. and Talley, L. D.: Hydrography of the eastern tropical Pacific: A review, Prog. Oceanogr., 69, 143–180, doi:10.1016/j.pocean.2006.03.008, 2006.

Grodsky, S. A., Carton, J. A., and Bentamy, A.: Salty anomalies forced by Tehuantepec and Papagayo gap winds: Aquarius observations, Remote Sens. Lett., 5, 568–574, doi:10.1080/2150704X.2014.935522, 2014.

Ishii, M., Feely, R. A., Rodgers, K. B., Park, G.-H., Wanninkhof, R., Sasano, D., Sugimoto, H., Cosca, C. E., Nakaoka, S., Telszewski, M., Nojiri, Y., Mikaloff Fletcher, S. E., Niwa, Y., Patra, P. K., Valsala, V., Nakano, H., Lima, I., Doney, S. C., Buitenhuis, E. T., Aumont, O., Dunne, J. P., Lenton, A., and Takahashi, T.: Air-sea CO$_2$ flux in the Pacific Ocean for the period 1990–2009, Biogeosciences, 11, 709–734, doi:10.5194/bg-11-709-2014, 2014.

Kerr, Y. H., Waldteufel, P., Wigneron, J. P., Delwart, S., Cabot, F. O., Boutin, and Escorihuela, M.: The SMOS mission: New tool for monitoring key elements of the global water cycle, Proc. IEEE, 98, 666–687, 2010.

Kessler, W.: Mean three-dimensional circulation in the northeast tropical Pacific, J. Phys. Oceanogr., 2457–2471, 2002.

Kessler, W. S.: The circulation of the eastern tropical Pacific: A review, Prog. Oceanogr., 69, 181–217, 2006.

Landschützer, P., Gruber, N., Bakker, D. C. E., and Schuster, U.: Recent variability of the global ocean carbon sink, Global Biogeochem. Cy., 28, 927–949, 2014.

Le Quéré, C., Moriarty, R., Andrew, R. M., Peters, G. P., Ciais, P., Friedlingstein, P., Jones, S. D., Sitch, S., Tans, P., Arneth, A., Boden, T. A., Bopp, L., Bozec, Y., Canadell, J. G., Chini, L. P., Chevallier, F., Cosca, C. E., Harris, I., Hoppema, M., Houghton, R. A., House, J. I., Jain, A. K., Johannessen, T., Kato, E., Keeling, R. F., Kitidis, V., Klein Goldewijk, K., Koven, C., Landa, C. S., Landschützer, P., Lenton, A., Lima, I. D., Marland, G., Mathis, J. T., Metzl, N., Nojiri, Y., Olsen, A., Ono, T., Peng, S., Peters, W., Pfeil, B., Poulter, B., Raupach, M. R., Regnier, P., Rödenbeck, C., Saito, S., Salisbury, J. E., Schuster, U., Schwinger, J., Séférian, R., Segschneider, J., Steinhoff, T., Stocker, B. D., Sutton, A. J., Takahashi, T., Tilbrook, B., van der Werf, G. R., Viovy, N., Wang, Y.-P., Wanninkhof, R., Wiltshire, A., and Zeng,

N.: Global carbon budget 2014, Earth Syst. Sci. Data, 7, 47–85, doi:10.5194/essd-7-47-2015, 2015.

Liss, P. and Johnson., M.: Ocean-Atmosphere Interactions of Gases and Particles, Springer-Verlag, Berlin, 55–112, 2014.

Park, G.-H., Wanninkhof, R. I. K., Doney, S. C., Takahashi, T., Lee, K., Feely, R. A., Sabine, C. L., Triñanes, J., and Lima, I. D.: Variability of global net sea–air CO_2 fluxes over the last three decades using empirical relationships, Tellus B, 62, 352–368, doi:10.1111/j.1600-0889.2010.00498.x, 2010.

Rangama, Y., Boutin, J., Etcheto, J., Merlivat, L., Takahashi, T., Delille, B., Frankignoulle, M., and Bakker, D. C. E.: Variability of the net air–sea CO_2 flux inferred from shipboard and satellite measurements in the Southern Ocean south of Tasmania and New Zealand, J. Geophys. Res.-Oceans, 110, C09005, doi:10.1029/2004JC002619, 2005.

Reul, N., Fournier, S., Boutin, J., Hernandez, O., Maes, C., Chapron, B., Alory, G., Quilfen, Y., Tenerelli, J., Morisset, S., Keer, Y., Mecklenburg, S., and Delwart, S.: Sea Surface Salinity Observations from Space with the SMOS Satellite: A New Means to Monitor the Marine Branch of the Water Cycle, Surv. Geophys., 35, 681–722, doi:10.1007/s10712-013-9244-0, 2013.

Rödenbeck, C., Keeling, R. F., Bakker, D. C. E., Metzl, N., Olsen, A., Sabine, C., and Heimann, M.: Global surface-ocean $p\text{CO}_2$ and sea–air CO_2 flux variability from an observation-driven ocean mixed-layer scheme, Ocean Sci., 9, 193–216, 2013, http://www.ocean-sci.net/9/193/2013/.

Sweeney, C., Gloor, E., Jacobson, A. R., Key, R. M., McKinley, G., Sarmiento, J. L., and Wanninkhof, R.: Constraining global air-sea gas exchange for CO_2 with recent bomb ^{14}C measurements, Global Biogeochem. Cy., 21, doi:10.1029/2006GB002784, 2007.

Takahashi, T., Sutherland, S. C., Wanninkhof, R., Sweeney, C., Feely, R. A., Chipman, D. W., and De Baar, H. J.: Climatological mean and decadal change in surface ocean $p\text{CO}_2$, and net sea–air CO_2 flux over the global oceans, Deep-Sea Res. Pt. II, 56, 554–577, 2009.

Takahashi, T., Sutherland, S. C., Chipman, D. W., Goddard, J. G., and Ho, C.: Climatological distributions of pH, $p\text{CO}_2$, total CO_2, alkalinity, and CaCO_3 saturation in the global surface ocean, and temporal changes at selected locations, Mar. Chem., 164, 95–125, 2014.

Turk, D., Zappa, C. J., Meinen, C. S., Christian, J. R., Ho, D. T., Dickson, A. G., and McGillis, W. R.: Rain impacts on CO_2 exchange in the western equatorial Pacific Ocean, Geophys. Res. Lett., 37, doi:10.1029/2010GL045520, 2010.

Wanninkhof, R.: Relationship between wind speed and gas exchange, J. Geophys. Res, 97, 7373–7382, 1992.

Weiss, R. F.: Carbon dioxide in water and seawater: The solubility of a nonideal gas, Mar. Chem., 2, 203–215, 1974.

Xie, S.-P., Xu, H., Kessler, W. S., and Nonaka, M.: Air–Sea Interaction over the Eastern Pacific Warm Pool: Gap Winds, Thermocline Dome, and Atmospheric Convection, J. Clim., 18, 5–20, 2005.

Zhao, M., Heinsch, F. A., Nemani, R. R., and Running, S. W.: Improvements of the MODIS terrestrial gross and net primary production global data set, Remote Sens. Environ., 95, 164–176, 2005.